Short-Lag Spatial Coherence of Backscattered Echoes: Imaging Characteristics

Muyinatu A. Lediju, Gregg E. Trahey, Brett C. Byram, and Jeremy J. Dahl

Abstract—Conventional ultrasound images are formed by delay-and-sum beamforming of the backscattered echoes received by individual elements of the transducer aperture. Although the delay-and-sum beamformer is well suited for ultrasound image formation, it is corrupted by speckle noise and challenged by acoustic clutter and phase aberration. We propose an alternative method of imaging utilizing the short-lag spatial coherence (SLSC) of the backscattered echoes. Compared with matched B-mode images, SLSC images demonstrate superior SNR and contrast-to-noise ratio in simulated and experimental speckle-generating phantom targets, but are shown to be challenged by limited point target conspicuity. Matched B-mode and SLSC images of a human thyroid are presented. The challenges and opportunities of real-time implementation of SLSC imaging are discussed.

I. Introduction

IN ultrasound, spatial coherence is a measure of the similarity of backscattered echoes received by individual transducer elements at a given time, as a function of element separation. The spatial coherence of backscattered ultrasound waves is described by the van Cittert-Zernike (VCZ) theorem, a fundamental tenet of modern optics. The VCZ theorem predicts the mutual intensity (also termed spatial covariance or mutual coherence evaluated at zero delay) of a wave field produced by an incoherent source [1]. According to this theorem, the spatial covariance in an observation region is the scaled Fourier transform of the intensity distribution of an incoherent source.

Mallart and Fink [2] and Liu and Waag [3] discuss the VCZ theorem's applicability to pulse-echo ultrasonic imaging, where diffuse scatterers in the isochronous volume insonified by a transmit beam represent an incoherent source. At the transmit focus, the spatial covariance of uniformly backscattered echoes can be modeled as the autocorrelation of the transmit aperture. For a 1-D linear array with no apodization, spatial covariance is equal to a triangle function with a base that is twice the transmit aperture width. This theoretical model of spatial covariance has been compared with simulation and experimental results with notable agreement [2], [4]–[6]. Walker and Tra-

hey [7] utilized a k-space representation to predict spatial covariance and arrived at a similar result.

Although the spatial coherence of backscattered echoes is independent of frequency and focal depth (for a focused transmit aperture and a uniform target), it is affected by other parameters, such as transmit beam shape, scatterer characteristics, receiver directivity, aberrations, gross velocity errors, and element nonuniformities. These factors scale, alter, or invalidate theoretical predictions of spatial coherence. For example, broad transmit beams, focal errors, aberrations, and element nonuniformities shorten coherence lengths [2], [4], [5], [8]. When the transmit aperture is Gaussian apodized, coherence is increased between closely spaced elements and degraded at large element spacings [4]. Diffuse or coherent targets laterally displaced from the transmit beam will decrease coherence lengths.

Geiman *et al.* [9] used the inverse Fourier transform of measured spatial coherence functions to reconstruct *in vivo* fundamental and harmonic transmit beam patterns and to experimentally demonstrate the effect of phase aberration on these beam patterns. Spatial coherence has also been used to derive analytical predictions of the performance of adaptive imaging methods. Methods that improve spatial coherence were shown to decrease aberration across an aperture, resulting in more accurate echo time-delay estimation [4].

Mallart and Fink [8] describe a coherence-based metric to analyze signals from scattering media. This metric, named the coherence factor by Hollman *et al.* [10], is a ratio of the coherent sum of signals across an aperture to the incoherent sum of these signals. The coherence factor describes focusing quality in the targeted medium. Li and Li [11] proposed an adaptive imaging technique based on a generalized version of the coherence factor. In this method, data containing high spatial frequencies across the receive array are excluded from the coherent sum. The exclusion of high spatial frequencies suppresses signals from off-axis targets or signals corrupted by phase aberration. The generalized coherence factor (GCF) is then calculated as the ratio of the modified coherent sum to the incoherent sum and is used to weight the beamsum before image formation. Variations of this method are described by Ustuner *et al.* [12]. Liu and Waag [13] describe a measure of waveform similarity that is similar to the coherence factor used by Li and Li [11]. Camacho *et al.* [14] utilized a phase coherence factor (PCF), which is based on the standard deviation of the phase of backscattered signals across the aperture, to weight the beamsum before image formation.

Bamber *et al.* [5] show a direct relationship between spatial coherence and receive beamformer gain. Gain is

The authors are with the Department of Biomedical Engineering, Duke University, Durham, NC (e-mail: muyinatu.lediju@duke.edu).

G. E. Trahey is also with the Department of Radiology, Duke University Medical Center, Durham, NC.

defined as the ratio between beamformer output power and the total power of echoes at each element. It may also be represented as the weighted area under Mallart and Fink's normalized spatial coherence function [5].

In this paper, a new approach to extracting useful information from spatial coherence functions is demonstrated, yielding images that have the potential to compete with conventional ultrasound B-mode images, particularly in cases where there is corruption caused by noise artifacts like clutter. Clutter originates from acoustic interactions with surrounding tissue (e.g., reverberation, off-axis scattering, phase aberration) [15]–[17], and it is a significant problem in numerous imaging environments, including vascular [18], cardiac [19], abdominal [20], and breast imaging [21], [22]. The proposed image processing method, described in Section II, is based on local measurements of the spatial coherence of backscattered echoes and is likely to have wide clinical utility in high-noise environments. Theory and simulation results obtained utilizing this method under various imaging conditions are explored. Experimental phantom and *in vivo* images based on this method are presented and compared with matched B-mode images (i.e., B-mode images created with the same data that was used to form the coherence-based images).

II. SHORT-LAG SPATIAL COHERENCE

For a receive aperture with N elements of equal spacing, the time-delayed signal received by the ith element is defined as $s_i(n)$, where n is the depth or time, in samples, and $s_i(n)$ is a zero-mean signal. The signals arriving across the receive aperture are time-delayed to ensure that the signals at sample n correspond to the same location. After time delay of the element signals, the estimated spatial covariance across the receive aperture is calculated as

$$\hat{C}(m) = \frac{1}{N-m} \sum_{i=1}^{N-m} \sum_{n=n_1}^{n_2} s_i(n)s_{i+m}(n), \qquad (1)$$

where m is the distance, or lag, in number of elements between two points in the aperture. Normalizing the covariance by the variance of the signals $s_i(n)$ and $s_{i+m}(n)$, the spatial correlation can be computed by

$$\hat{R}(m) = \frac{1}{N-m} \sum_{i=1}^{N-m} \frac{\sum_{n=n_1}^{n_2} s_i(n)s_{i+m}(n)}{\sqrt{\sum_{n=n_1}^{n_2} s_i^2(n)\sum_{n=n_1}^{n_2} s_{i+m}^2(n)}}. \qquad (2)$$

The choice of the normalizing term differs from that used by Mallart and Fink [2], who normalized (1) by the estimated spatial covariance at zero lag. However, both normalization terms serve the same purpose, in that the relative strengths of the echo signals are removed from the spatial covariance terms. Eq. (2) is identical to the spatial coherence calculation used by Fedewa *et al.* [23]. Although spatial covariance (1) and spatial correlation (2)
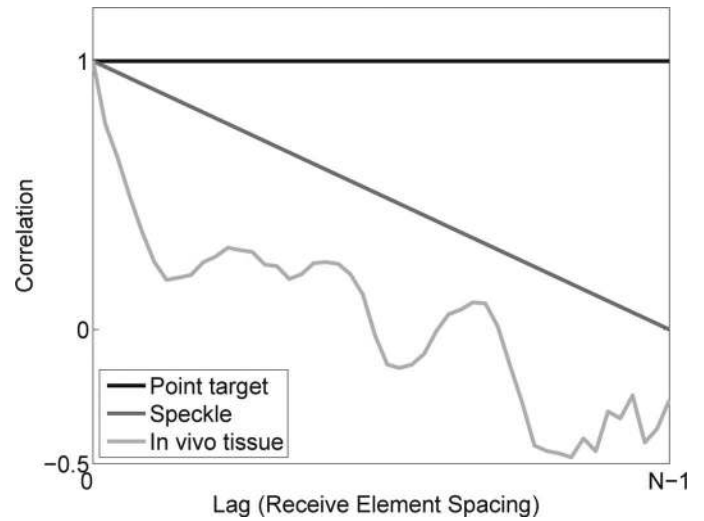

Fig. 1. Examples of coherence functions in a point target and speckle background, as well as an experimental coherence function from *in vivo* thyroid tissue. The abscissa represents the lag, or spacing between receive elements. The ordinate represents inter-element RF echo correlation.

have different definitions, the term spatial coherence refers to both (i.e., both are a measure of the similarity of backscattered echoes as a function of element separation). The term spatial coherence will be used hereafter in reference to (2), and spatial covariance is used in reference to (1).

Fig. 1 illustrates the normalized theoretical spatial covariance across the receive aperture for a point target positioned at the transmit focus and uniformly-distributed diffuse scatterers, compared with the spatial coherence of *in vivo* echoes from a human thyroid. For a point target, the source function is modeled as an impulse, so the spatial coherence is constant across the aperture. For diffuse scatterers, the source function is modeled as a constant, and the source intensity distribution (i.e., the square of the lateral transmit beam shape) is modeled as a squared sinc function. The corresponding expected spatial coherence function is a triangle, or a line decreasing from 1 at zero lag to 0 at lag $N-1$, where N refers to the number of elements in the transmit aperture, which is assumed to be identical to the receive aperture for simplicity. The spatial coherence of *in vivo* tissue from a human thyroid is expected to be similar to that of diffuse scatterers. However, the coherence demonstrated in Fig. 1 indicates that there is underlying corruption of the signals (e.g., reverberation clutter, strong off-axis targets, phase aberration, or electronic noise) that decreases spatial coherence across the aperture.

For a given transmit beam shape, the spatial coherence will vary depending on the lateral backscatter distribution and the amount of signal corruption. Although it is difficult to increase spatial coherence above the predicted coherence for diffuse scatterers without a strongly reflecting and/or a laterally compact target at the transmit focus, a decrease in spatial coherence below the expected value for diffuse targets is relatively easy to obtain via increased

noise or decreased on-axis source strength. In this case, the largest losses in spatial coherence will occur in the regions of low lags, or in the coherence between closely-separated elements, as has been observed in the spatial coherence of backscattered signals with phase aberration [4]. We therefore describe a metric, called the short-lag spatial coherence (SLSC), as the integral of the spatial coherence function over the first M lags:

$$R_{\text{sl}} = \int\limits_{1}^{M} \hat{R}(m) \mathrm{d}m \approx \sum_{m=1}^{M} \hat{R}(m). \quad (3)$$

Given that coherence functions scale with the size of the transmit aperture, a parameter Q is introduced to report values of M as a percentage of the transmit aperture width, where

$$Q = \frac{M}{N} \times 100\%. \quad (4)$$

Q ranges from 1 to 30% for our proposed realizations of SLSC imaging.

III. Methods

To evaluate the characteristics of images created using the short-lag spatial coherence, simulated images using Field II [24] were created. A numerical computation of the SLSC image at the focal depth, based on the theoretical spatial coherence, was compared with the simulated images. SLSC images of tissue-mimicking phantoms and *in vivo* human thyroid were also generated to demonstrate the potential application to clinical imaging.

A. Theoretical Prediction of Short-Lag Spatial Coherence

The spatial covariance of wavefronts across an aperture can be predicted by the Fourier transform of the square of the product of the lateral transmit beam pressure and the lateral backscatter, or source, function [2]. In mathematical notation, spatial covariance is given by

$$C(u,v) = \int_{-\infty}^{\infty}\int_{-\infty}^{\infty} |\chi(x,y)H(x,y)|^2 \, \mathrm{e}^{-j2\pi(xu+yv)} \mathrm{d}x\mathrm{d}y, \quad (5)$$

where x and y are the spatial dimensions in the source plane, $\chi(x,y)$ is the source (or scattering) function, $H(x,y)$ is the transmit beam amplitude, and u and v are spatial frequencies evaluated at $u = x'/\lambda z$ and $v = y'/\lambda z$. The variable x' is the spatial difference between two points in the x dimension of the aperture plane, y' is the spatial difference between two points in the y dimension of the aperture plane, z is the distance between the source and the aperture planes, and λ is the ultrasonic wavelength.

To predict the lateral profiles of SLSC images at the focal depth, the lateral transmit beam amplitude, $H(x)$, was modeled as a sinc function based on the parameters in

TABLE I. Simulated Transducer Parameters.

Parameter	Value
Number of elements	96
Element height	7.5 mm
Element width	0.176 mm
Kerf	0.025 mm
Center frequency	5.71 MHz
Sampling frequency	160 MHz
Fractional bandwidth	60%

Table I. For a lesion, the source function $\chi(x)$ was modeled as a constant minus a rectangular pulse, where the ratio of the pulse amplitude to the constant was equal to the contrast of the lesion and the width of the pulse was equal to the diameter of the lesion. Note that χ or H may be modified to arbitrary geometries, enabling theoretical predictions for other target types or transmit beam shapes.

The spatial covariance in the lateral dimension was numerically computed using the fast Fourier transform of $|H(x)\chi(x)|^2$. The spatial covariance was then normalized at zero lag and resampled at the spacing of the array elements to create a spatial coherence function. The theoretical short-lag spatial coherence was then calculated by integrating the resulting spatial coherence function over the first M lags, as described by (3). Noise was not considered in this numerical computation. Note that this description of short-lag spatial coherence is valid only at the focal depth of the transmit beam. Computation at other depths requires incorporation of the lateral intensity of the defocused transmit beam. There is no variance in predicted values because the theoretical model of the spatial coherence does not account for the randomness of diffuse scatterers.

B. Field II Simulations

Field II was used to simulate the received, individual-channel, echo signals from a variety of imaging targets. Three-dimensional phantoms containing a 3-mm spherical lesion and three point targets were utilized, where the contrast of the lesion was varied from anechoic to 6 dB. The point target brightness in each phantom was varied from 6 to 24 dB relative to the rms value of the diffuse scatterer strength. Each phantom measured 6 mm axially by 10 mm laterally by 10 mm in elevation and contained 20 scatterers per resolution volume. The simulated transducer was a linear array with a 5.7 MHz center frequency and 60% fractional bandwidth. The array had a lens focused at 3.75 cm in elevation, and the lateral focus was positioned at the same depth. An F/2 transmit aperture was employed and dynamic-receive beamformer delays were applied to the channel signals. No apodization was applied to the transmit aperture. The parameters of the simulated transducer are listed in Table I.

In Field II, regions that do not contain scatterers have low amplitude echoes in the received channel signals. These echoes are a few orders of magnitude below backscattered and off-axis echoes and often reside below

the noise floor seen in experimentally-obtained ultrasonic data. Because coherence calculations do not depend on signal magnitude, these low-amplitude echoes yield coherence estimates unlikely to be observed in experimental measurements. Therefore, uniform white noise was band-pass filtered and added to the channel signals to suppress coherence from low-amplitude echoes created by Field II; the resulting SNR of the channel signals was 10 dB, comparable to that measured in *in vivo* data [25]. The cutoff frequencies used in the band-pass filter were equal to the −6-dB bandlimits of the transducer to simulate acoustic noise received by the transducer. Introducing incoherent noise with amplitudes greater than the spurious echoes suppresses artifacts in the simulated images and adds a degree of realism to the echo signals.

To analyze the lateral resolution of SLSC images, a numerical differentiation technique described in [26] is employed because conventional techniques, such as the autocorrelation of speckle or the width of a point target, are not practical because of the spurious echoes described previously. In this method, two phantoms, each containing two adjacent vertical regions of differing contrast, were used to compute a spatial step function. For B-mode resolution calculations, one of the vertical regions was anechoic. For SLSC resolution calculations, the backscatter difference between the two regions was 12 dB. To determine lateral resolution, an estimated lateral point spread function (PSF) was created by numerical differentiation of the step function, and the width of the resulting PSFs was measured at −6 and −10 dB.

To study SLSC imaging characteristics of expanded targets, six independent speckle realizations of a 1-cm spherical lesion phantom were simulated, using the transducer parameters listed in Table I. The contrast of the lesion was −9.8 dB, which was chosen to match the phantom experiment described in Section III-C. Each phantom measured 15 mm axially by 30 mm laterally by 1 mm in elevation and contained 20 scatterers per resolution volume. The simulated transducer array had a lens focused at 3.75 cm in elevation, and the lateral focus was positioned at the same depth. An F/2 transmit aperture was employed and dynamic-receive beamformer delays were applied to the channel signals. No apodization was applied to the transmit aperture. Simulations were performed with and without noise that was 10 dB down from the channel signals.

C. Tissue-Mimicking Phantoms and In Vivo Experiments

An RMI 408 Spherical Lesion Phantom (Gammex RMI, Middleton, WI) containing 4-mm anechoic lesions spaced 1 cm apart was used as an imaging target to compare B-mode and SLSC imaging. Individual channel signals were acquired on a VF10–5 linear array transducer (Siemens Medical Solutions USA Inc., Issaquah, WA) attached to a Siemens Antares ultrasound scanner (Siemens Medical Solutions USA Inc.). The transmit frequency was 8.0 MHz, and the number of transmit elements was adjusted to maintain a constant F/2 transmit. Individual

channel signals were acquired using the Axius Direct Diagnostic User Interface (Siemens Medical Solutions USA Inc.) [27] in conjunction with a synthetic receive aperture technique [25]. Signals were acquired with a transmit focus of 2.0 cm. The total number of receive elements in the array was 192, however only echoes from the 64 elements centered about the transmit aperture for that beam were acquired. Individual channel signals were acquired for 54 A-lines. Dynamic-receive beamforming delays were applied to the channel signals.

A contrast-detail phantom (ATS Laboratories, Bridgeport, CT), described by Smith and Lopez [28], was utilized to image a 1-cm cross-section of a conical lesion. An identical setup to the RMI phantom experiments was employed, except that a VF7–3 linear array transducer was used with a center frequency of 5.7 MHz and a transmit focus of 3.75 cm. Echoes from 64 elements were acquired for 108 A-lines.

In vivo individual channel data from the thyroid of a 34-year-old male volunteer were acquired in addition to phantom data. An identical setup to the RMI phantom experiments was employed, except that 48 receive elements centered about the transmit aperture were used to acquire three sets of individual channel signals, each with a unique transmit focus of 0.5, 1.5, or 2.5 cm.

D. Coherence Image Processing

The short-lag spatial coherence was computed for simulated, phantom, and *in vivo* data using (2) and (3). SLSC images were formed by computing the short-lag spatial coherence at each depth n of each A-line, using a correlation kernel size (i.e., $n_2 - n_1$) of one wavelength. The size of the correlation kernel impacts the quality of the correlation calculation as well as the axial resolution of SLSC images. A kernel size of one wavelength was chosen to maintain an axial resolution that is comparable to B-mode images, yet produce stable coherence functions. B-mode images were constructed with the same individual channel data using conventional delay-and-sum methods. The contrast (C), contrast-to-noise ratio (CNR), and speckle signal-to-noise ratio (SNR) in the B-mode and SLSC images were calculated using the following equations:

$$C = 20 \log_{10}\left(\frac{S_i}{S_o}\right), \qquad (6)$$

where S_o and S_i are the mean signals at the same depth outside and inside a lesion, respectively.

$$CNR = \frac{|S_i - S_o|}{\sqrt{\sigma_i{}^2 + \sigma_o{}^2}}, \qquad (7)$$

where σ_o and σ_i are the standard deviations of signals at the same depth outside and inside a lesion, respectively.

$$SNR = \frac{S_o}{\sigma_o}. \qquad (8)$$

Point target conspicuity in simulated images was calculated using

$$\text{Conspicuity} = \frac{S_{\max} - S_{\mathrm{o}}}{\sigma_{\mathrm{o}}}, \qquad (9)$$

where $S_{\max}$ is the peak brightness of the point target and S_{o} and σ_{o} are the mean brightness and standard deviation, respectively, of a background region at the same depth as the point target. All image processing and data analysis was performed with Matlab (The MathWorks Inc., Natick, MA) software.

IV. RESULTS

A. Field II Simulations

Matched B-mode and SLSC images are displayed in Fig. 2. The first row shows B-mode images with anechoic, -24-dB-contrast, and -18-dB-contrast lesions, from left to right. The second row shows B-mode images with lesion contrasts of -12, -6, and 6 dB, from left to right. Corresponding SLSC images created with Q equal to 20.8% are shown in rows three and four. The B-mode and SLSC images show 40 dB of dynamic range. Identical regions from all images (indicated by the white boxes in the upper-left image) were used to calculate contrast, CNR, SNR, and point target conspicuity. Visual inspection of the SLSC images reveals similarity to the corresponding B-mode images, however there is a significant loss in visualization of the point targets. The variance in the background region appears to be reduced as well.

Measured contrast and CNR of the simulated lesions, as a function of lesion contrast, are displayed in Fig. 3. Contrast of the lesions in the B-mode images has excellent agreement with ideal values (i.e., the intrinsic contrast of the lesions). At $Q = 5.2\%$, contrast is reduced in SLSC images compared with B-mode images. However when Q was increased to 20.8%, the contrast in the SLSC and B-mode images is similar. CNR increased significantly in the SLSC images compared with B-mode images as a result of a large increase in SNR. The average SNR at the focal depth in the B-mode images is 2.1 ± 0.3 and in the SLSC images formed with Q equal to 5.2% and 20.8% is 11.3 ± 2.2 and 5.7 ± 0.9, respectively. Point target conspicuity as a function of point target brightness is displayed in Fig. 4. Conspicuity increases with target brightness in B-mode images, but remains flat and significantly lower in SLSC images. SLSC results are shown for $Q = 20.8\%$, but are nearly identical for $Q = 5.2\%$.

In Fig. 5, simulated B-mode and SLSC images without added noise are compared with a numerical computation of the theoretical SLSC image. Six independent realizations of simulated B-mode and SLSC images were averaged to reduce background variance for a better comparison with theory. The averaged B-mode image was normalized to the same scale as the theoretical SLSC image. There is good agreement between simulated and theoretical SLSC images.

Figs. 6(a) and 6(b), respectively, show the contrast and CNR of the -24-dB lesion in SLSC and B-mode images as a function of Q, where Q refers to the percent of the transmit aperture for SLSC and B-mode images. Contrast in SLSC images is optimal for Q greater than 20%. Contrast in B-mode images improves with an increasing number of receive elements. The CNR of SLSC images peaks at $Q = 10.4\%$, however CNR is relatively flat for B-mode images. Fig. 6(c) shows SNR as a function of Q. Predictably, the SNR in B-mode images is unchanged as a function aperture size, but SNR in the SLSC images decreases with increasing Q and is up to an order of magnitude higher than that of B-mode images.

Fig. 6(d) shows lateral resolution at -6 and -10 dB as a function of Q, as measured with the numerical differentiation technique. Compared with resolution values measured using the lateral width of a simulated point target (not shown), the reported B-mode image resolution values reflect better resolution by an average of 0.13 and 0.18 mm at -6 and -10 dB, respectively. Although similar biases are suspected in SLSC resolution calculations, the trends observed using this method are expected to be valid. These trends include a general improvement in lateral resolution with increasing Q and slightly better resolution in SLSC images compared with B-mode images of equivalent-sized apertures, particularly at -6 dB.

The lateral resolution of SLSC images at $Q = 20.8\%$ (i.e., the same Q used to make the SLSC images in Fig. 2) is 0.47 and 0.63 mm at -6 and -10 dB, respectively, as reported in Fig. 6(d). The lateral resolution of the B-mode images in Fig. 2, which were created with the entire transmit aperture, measured 0.43 and 0.55 mm at -6 and -10 dB, respectively, using the numerical differentiation technique. Using the lateral width of a simulated point target, lateral resolution measured 0.50 and 0.65 mm at -6 and -10 dB, respectively.

The axial resolution of the coherence images is approximately equal to the correlation kernel length convolved with half the pulse length, as in correlation-based imaging techniques such as ARFI [29], [30] and elastography [31], [32]. In all SLSC images, the correlation kernel length was equal to λ.

B. Experiments in Tissue-Mimicking Phantom

Matched B-mode and SLSC images (Q equal to 7.8%, 15.6%, and 23.4%) of the RMI spherical lesion phantom are shown in Fig. 7 and demonstrate changes in image characteristics with increasing Q. SLSC images have increased focal gain with increasing Q, but lesions are still easily visualized, with the exception of the shallower lesions. In addition, lesion boundaries appear sharper with increasing Q, an indication of increased resolution.

Contrast and CNR of the focal lesion and SNR at the focus of B-mode and SLSC images in Fig. 7 are reported in Table II. The differences in contrast are marginal for the three SLSC images, but CNR and SNR decrease with increasing Q.
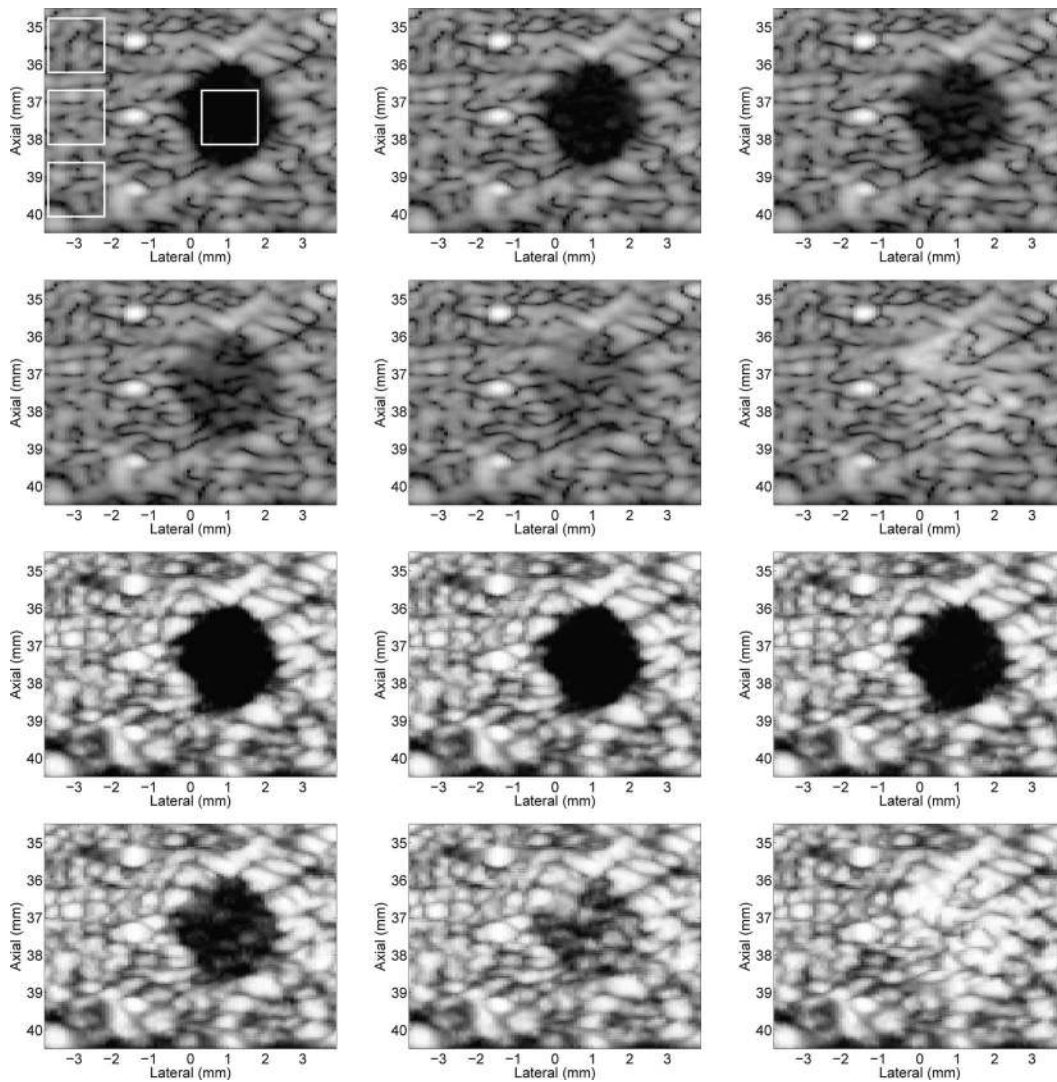
Fig. 2. Simulated B-mode images of 3-mm lesions with contrasts of anechoic, −24, −18 dB from left to right in the first row, and 6 dB from left to right in the second row. The corresponding SLSC images created with $Q = 20.8\%$ are shown in rows 3 and 4. B-mode and SLSC images are shown with 40 dB of dynamic range. The boxes in the upper-left image indicate ROIs used to calculate the contrast, CNR, SNR, and point target conspicuity.
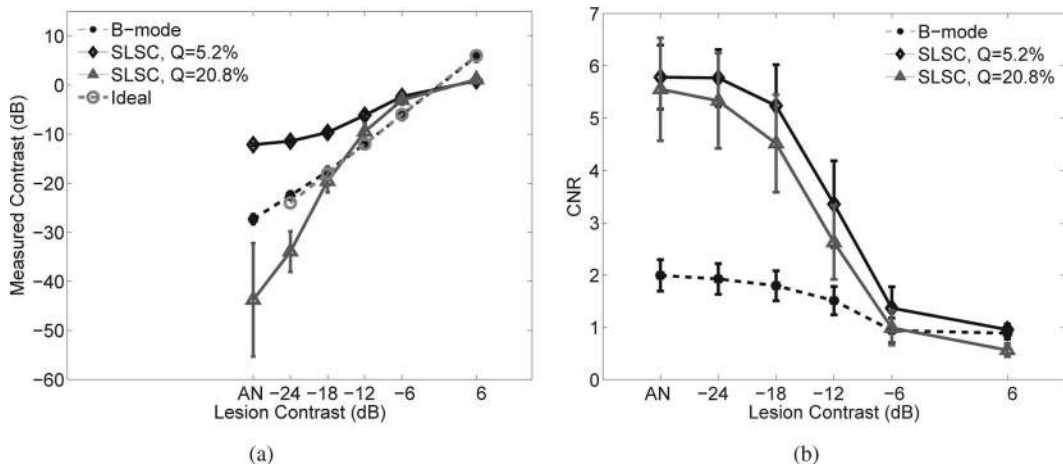

Fig. 3. Mean (a) contrast and (b) CNR observed in the lesions of the simulated B-mode and SLSC images, as a function of the intrinsic lesion contrast. Contrasts of the B-mode images are a close match to ideal values. SLSC imaging suffers a significant decrease in contrast when $Q = 5.2\%$, but is more similar to B-mode imaging when $Q = 20.8\%$. SLSC imaging with $Q = 5.2\%$ and 20.8% shows considerably higher CNR for hypoechoic lesions than B-mode imaging. Error bars indicate one standard deviation.
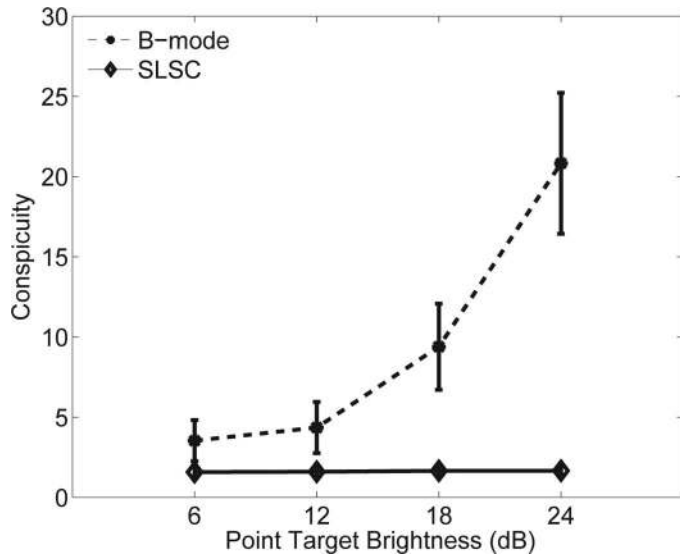
Fig. 4. Point target conspicuity increases as a function of target brightness for B-mode imaging, but remains flat for SLSC imaging regardless of brightness or Q. Error bars indicate one standard deviation.
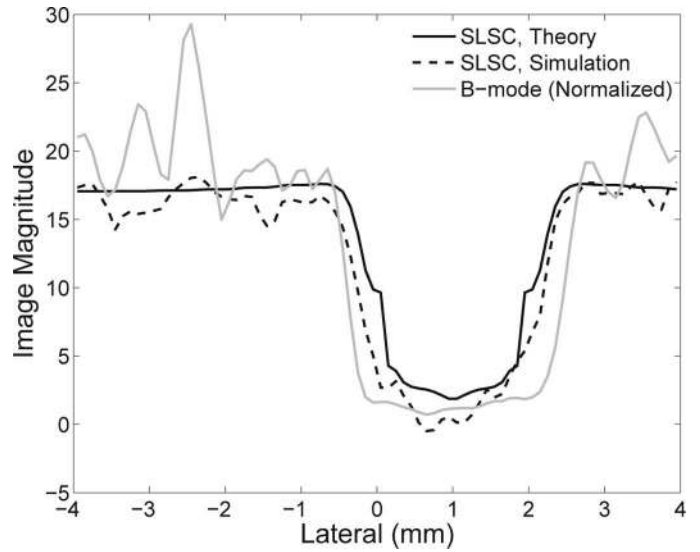

Fig. 5. Theoretical calculations of the short-lag spatial coherence image compared with the simulated B-mode and SLSC images for a lateral slice through the center of a spherical 3-mm anechoic lesion with -24 dB contrast.
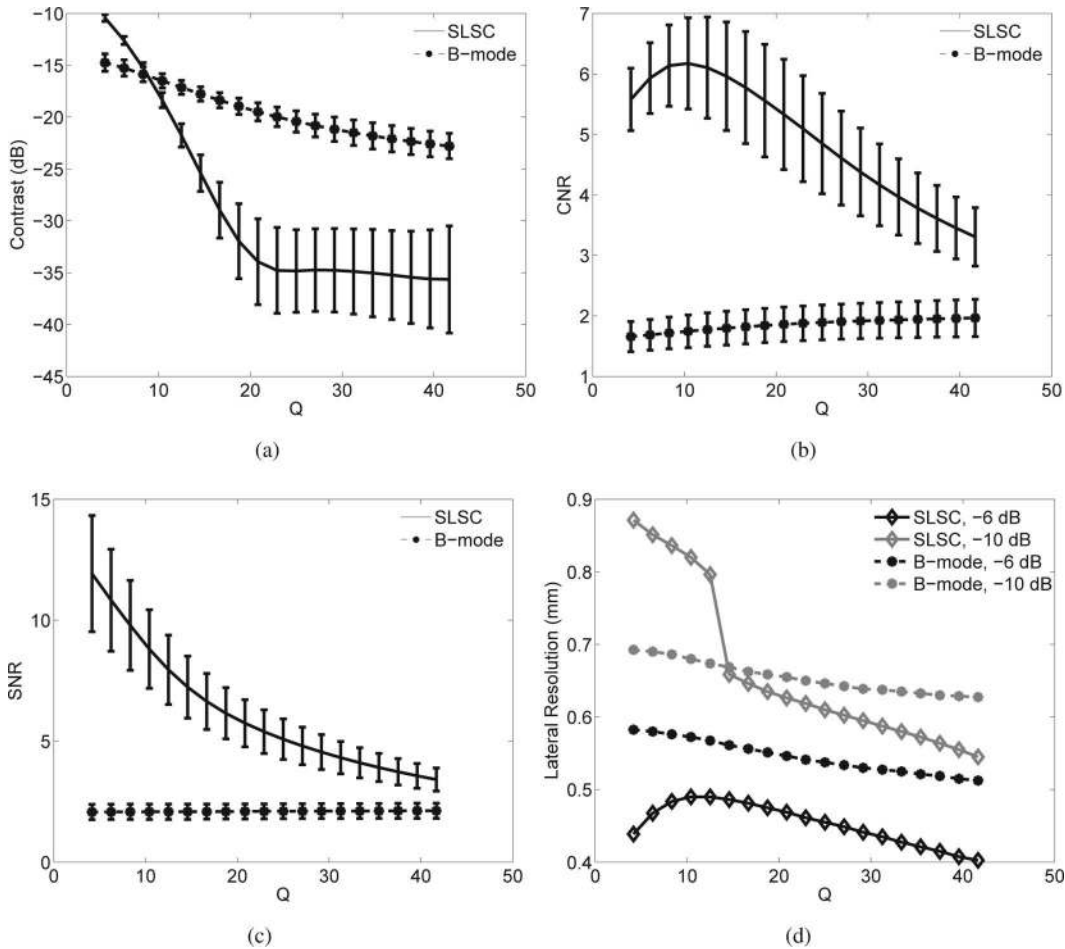

(a)

(b)

(c)

(d)

Fig. 6. (a) Contrast and (b) CNR for the -24 dB lesion, (c) SNR, and (d) lateral resolution as a function of Q. Q indicates the size of the receive aperture, expressed as a percentage of the transmit aperture used to create the SLSC and B-mode images. Error bars indicate one standard deviation for six simulations.
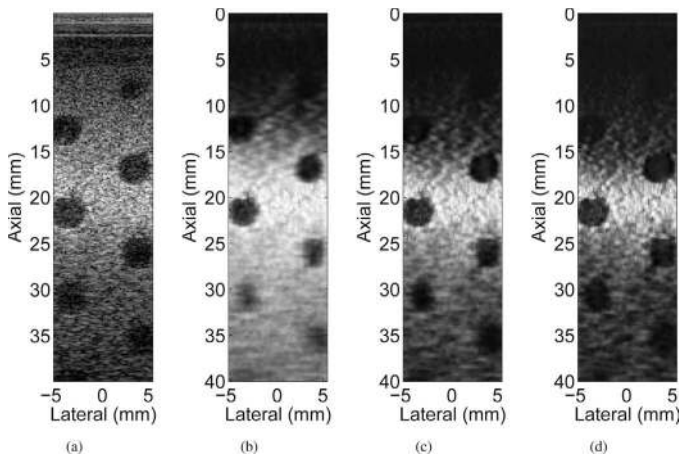
Fig. 7. Matched (a) B-mode and (b)–(d) SLSC images of 4-mm spherical anechoic lesions in a tissue-mimicking phantom. The SLSC images were created with Q equal to 7.8, 15.6, and 23.4%, from left to right, respectively. The SLSC images show improved CNR and SNR and increased depth-of-field effects for smaller Q. Resolution differences are observable with increasing Q.

C. SLSC of Expanded Targets

Matched B-mode and SLSC images of the simulated and experimental 1-cm lesion are shown in Fig. 8. In the simulated SLSC image [Fig. 8(b)], the lesion is well visualized but has lower contrast compared with the corresponding B-mode image [Fig. 8(a)]. Although the lesion borders are well defined, the center of the lesion shows more coherence than the borders, resulting in lower contrast and CNR when compared with the matched B-mode image. This image characteristic will be referred to as recorrelation. The experimental SLSC image [Fig. 8(d)] does not appear to have the recorrelation characteristic. The contrast, CNR, and SNR of lesions in Fig. 8 were calculated using the ROIs shown, and the values are listed in Table II.

Averaged lateral profiles about the focus of the simulated B-mode and SLSC images from Fig. 8 are compared with the theoretical computation of the SLSC profile in Fig. 9(a). Six independent realizations of simulated B-mode and SLSC images were averaged to reduce background variance for a better comparison with theory. The simulated SLSC and B-mode profiles were normalized by the mean of the background. There is good agreement between simulated and theoretical SLSC images, as the lesion center in both images has more coherence than its borders (i.e., they both have the recorrelation effect).

Fig. 9(b) shows lateral profiles about the focus for the experimental 1-cm lesion displayed in Figs. 8(c) and 8(d). The experimental SLSC profiles do not show recorrelation at the lesion center and are more similar to the SLSC simulation results with added noise. Note that the addition of noise to the simulation eliminates the recorrelation effect and increases the contrast and CNR of the lesion. Contrast, CNR, and SNR at the focus of the simulated images with noise are reported in Table II.

TABLE II. Contrast, CNR, and SNR at Focus of Experimental Phantom, Simulated, and *In Vivo* Thyroid Data.

|	Contrast (dB)	CNR	SNR
Experimental phantom images, 3-mm lesions			
B-mode	−17.3	1.6	1.7
SLSC, $Q = 7.8\%$	−13.6	6.4	15.8
SLSC, $Q = 15.6\%$	−14.3	6.9	9.0
SLSC, $Q = 23.4\%$	−14.3	6.0	6.2
Simulation images with no noise, 1-cm lesions (mean ± s.d.)			
B-mode	−10.0 ± 0.6	1.2 ± 0.1	1.9 ± 0.0
SLSC, $Q = 6.3\%$	−0.5 ± 0.1	1.2 ± 0.1	128.9 ± 8.7
SLSC, $Q = 10.4\%$	−1.1 ± 0.1	1.2 ± 0.1	45.6 ± 2.6
SLSC, $Q = 20.8\%$	−1.2 ± 0.2	0.9 ± 0.1	16.0 ± 0.8
Simulation images with noise, 1-cm lesions (mean ± s.d.)			
B-mode	−9.9 ± 0.7	1.2 ± 0.1	1.9 ± 0.0
SLSC, $Q = 6.3\%$	−5.0 ± 0.5	2.2 ± 0.2	11.7 ± 1.0
SLSC, $Q = 10.4\%$	−5.0 ± 0.5	2.2 ± 0.2	11.6 ± 1.0
SLSC, $Q = 20.8\%$	−4.9 ± 0.5	2.1 ± 0.2	10.5 ± 0.8
Experimental phantom images, 1-cm lesion			
B-mode	−9.8	1.1	1.9
SLSC, $Q = 12.5\%$	−8.4	2.1	9.9
SLSC, $Q = 21.9\%$	−7.5	2.1	10.8
SLSC, $Q = 31.3\%$	−6.7	2.1	10.2
In vivo thyroid images			
B-mode	−20.3	1.9	2.1
SLSC, $Q = 10.4\%$	−37.7	5.3	5.8
SLSC, $Q = 20.8\%$	−56.7	4.0	4.2
SLSC, $Q = 31.2\%$	−44.8	3.1	3.2
Spatial-compounded	−14.4	2.8	3.5
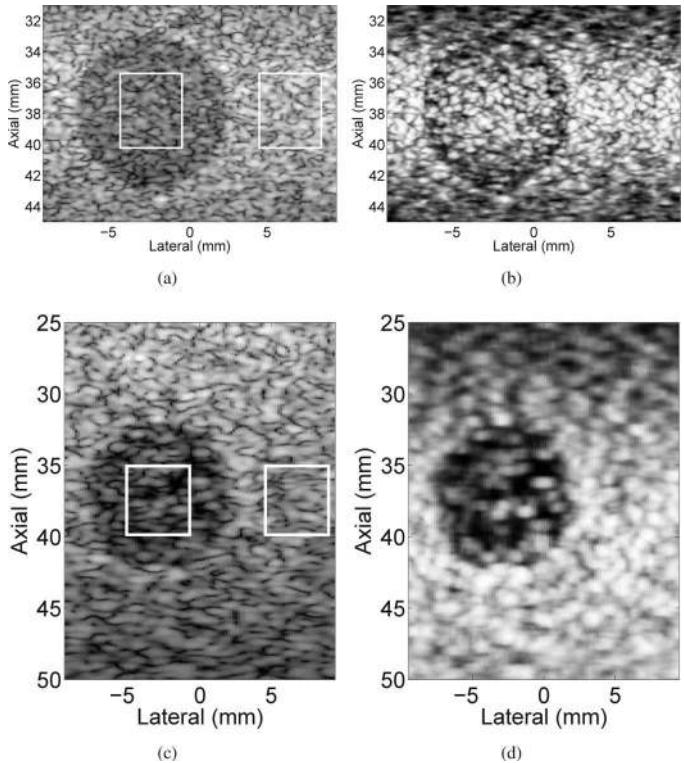
Fig. 8. Matched B-mode (left) and SLSC (right) images of 1-cm lesions, formed from simulated data without noise (top) and experimental data (bottom). Q is equal to 20.8% and 20.3% in simulated and experimental data, respectively. The boxes indicate ROIs used to calculate the contrast, CNR, and SNR. B-mode and SLSC images are shown with 50 dB dynamic range.
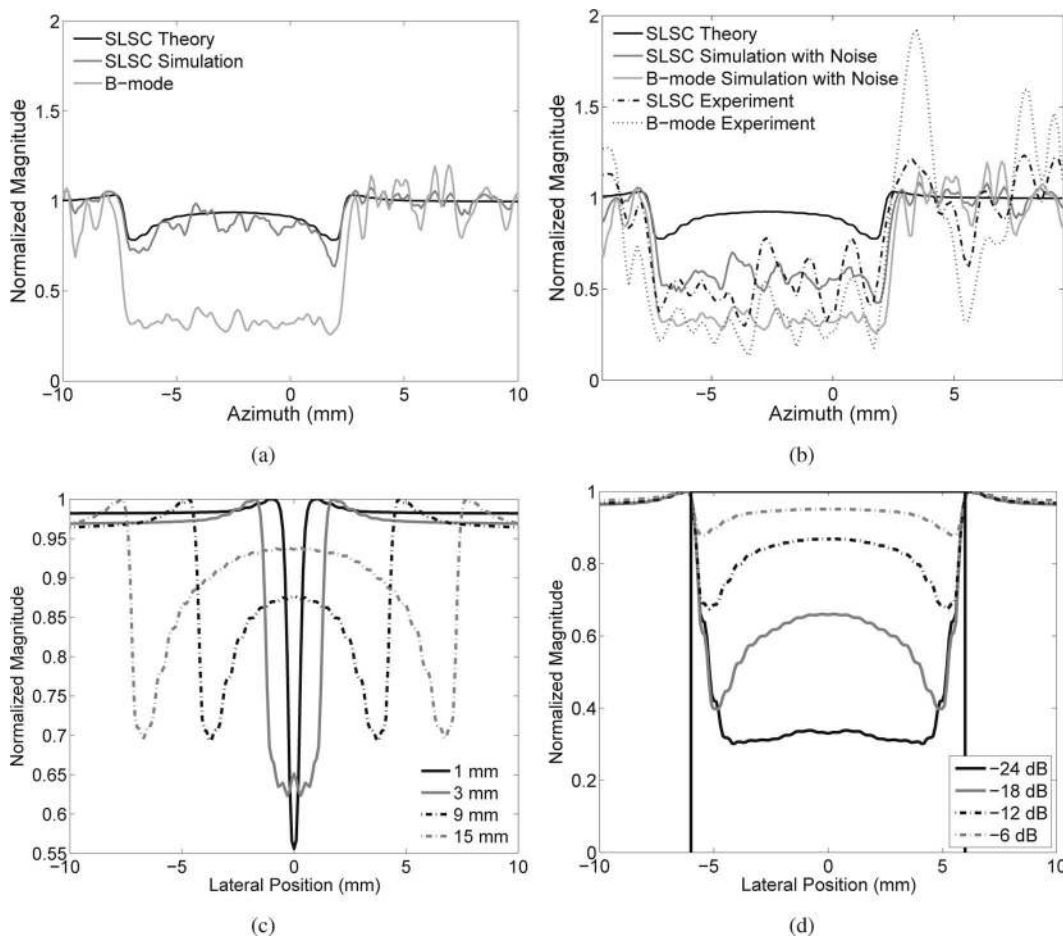
Fig. 9. Theoretical calculations of the short-lag spatial coherence image. A lateral slice through the center of a spherical 1-cm lesion with -12 dB contrast is compared with simulated data with no noise (a), simulated data with noise, and experimental data (b). (c) Theoretical -12 dB contrast lesions of varying sizes. (d) Theoretical 12-mm lesions of varying contrasts, with the vertical lines denoting lesion boundaries. Q is equal to 20.8% in theory and simulations and 20.3% in experimental data.

Fig. 9(c) illustrates theoretical predictions for various lesion sizes with the same -12-dB contrast, normalized by maximum values. Recorrelation is not apparent in small lesions. In larger lesions, the recorrelation effect increases with lesion size.

Fig. 9(d) demonstrates theoretical predictions for 12-mm lesions with differing contrasts. The amount of recorrelation changes as a function of the intrinsic lesion contrast.

D. In Vivo Human Thyroid Images

In vivo B-mode, SLSC (Q equal to 10.4%, 20.8%, and 31.2%), and spatial-compounded images of a human thyroid are shown in Fig. 10. Each image was created from data acquired at three transmit foci and blended to form a single image. The spatial-compounded image was created from 43 B-mode images with coherent receive apertures equal to 10.4% of the transmit aperture and spaced 2.1% of the transmit aperture apart. A cyst is visible in the thyroid at 1.5 cm depth. The B-mode, SLSC, and spatial-compounded images are shown with 50 dB of dynamic range.

Contrast and CNR of the cyst and SNR of the thyroid tissue at 1.5 cm are reported in Table II. Contrast is im-

proved by 17, 36, and 25 dB in the SLSC images formed with $Q = 10.4$, 20.8, and 31.2%, respectively, when compared with the B-mode image. Contrast in the spatial-compounded image is reduced by 6 dB compared with the B-mode image. CNR and SNR are greatest in SLSC images, particularly when $Q = 10.4$%, and decrease with increasing Q.

V. Discussion

The short lags of the spatial coherence function allow discrimination of imaging targets without direct utilization of echo brightness. Generally, bright diffuse scatterers have higher spatial coherence at short lags, when compared with adjacent anechoic regions. The source of contrast in SLSC images when two adjacent regions of diffuse scatterers only differ in magnitude is counterintuitive because the spatial coherence calculated by (2) has no dependence on echo brightness. Intuition might predict that the two backscattered echoes should have the same spatial coherence and therefore produce a uniform SLSC image. However, we hypothesize that off-axis echoes from
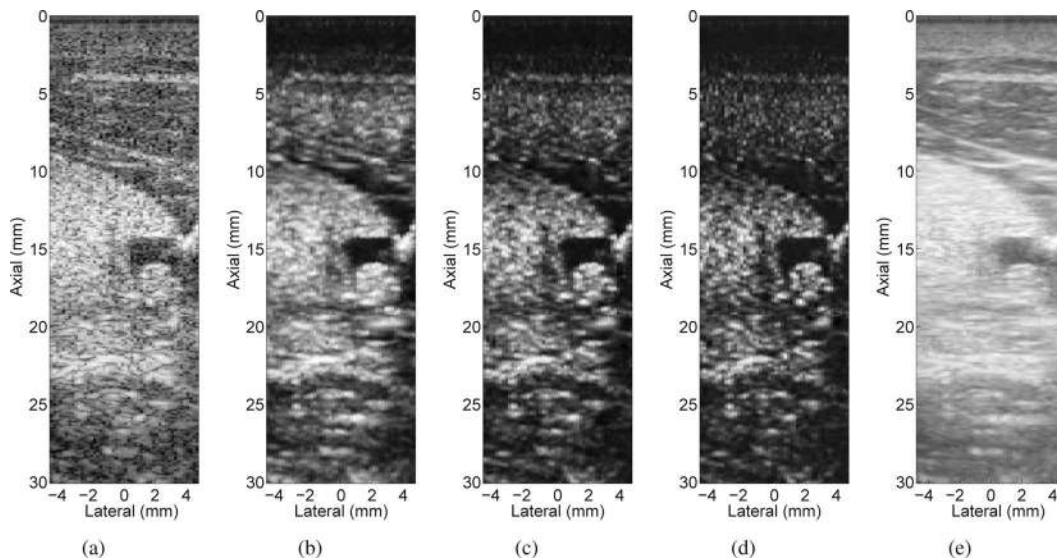
Fig. 10. (a) *In vivo* B-mode image of a cyst at 1.5 cm depth in a human thyroid. SLSC images of the thyroid formed with (b) $Q = 10.4\%$ (c) $Q = 20.8\%$, and (d) $Q = 31.2\%$. (e) A spatial-compounded image of the thyroid. The SLSC images show improved CNR of the cyst and improved SNR of the thyroid tissue compared with the B-mode and spatial-compounded images. The SLSC images also show improved resolution compared with the spatial-compounded image.

nearby higher-amplitude regions are added out of phase to echoes received from hypoechoic regions, thereby decreasing spatial coherence in hypoechoic regions, and thus generating contrast in SLSC images. As the distance between the main lobe of the transmit beam and the interface of the two regions increases, the contribution from interfering echoes diminishes and the coherence of on-axis signals in the hypoechoic region is increased. This recovery of the coherence is responsible for the recorrelation demonstrated in Figs. 8(b) and 9(a). Figs. 5 and 9 demonstrate that theoretical predictions and simulation results without noise are consistent with these hypotheses. Simulations with added noise and experimental results with intrinsic noise show mitigation of the recorrelation effect observed in noise-free environments. Moreover, the appearance of the recorrelation effect is dependent on the amount of noise added to simulated data. For this simulation, noise in the range of 6 dB down from the channel signals will show minimal recorrelation reduction, whereas noise as great as 20 dB eliminates the recorrelation effect.

There are four notable features of SLSC imaging. First, the SNR for regions of diffuse scatterers is markedly higher in SLSC images compared with B-mode images. This is due to the low variance at short lags of the spatial coherence function for diffuse scattering regions. The variance in the spatial coherence function is not easily modeled, however empirical determination of the variance shows that it typically increases with decreasing correlation for a diffuse scattering region. In addition, the variance is not evenly distributed about the mean and is skewed toward unity for the higher correlation coefficients.

Second, resolution is improved by increasing Q, as shown in Fig. 6(d) and evident in Figs. 7 and 10. The improved resolution is due to the addition of higher spatial frequency content from the larger lags of the receive

beamformer. Furthermore, SLSC images appear to have better lateral resolution than B-mode images formed with equivalent aperture sizes, as shown in Fig. 6(d) for simulated data and illustrated in Figs. 10(b) and 10(e) for experimental data.

Third, although the contrast of SLSC images generally improves with an increase in the number of lags summed, SNR improves with decreasing Q. There appears to be a trade-off among contrast, CNR, and SNR when selecting a value for Q. Nevertheless, the SNR of SLSC images is larger than that of B-mode images, and the large gain in CNR is due to the increased SNR of the background.

Fourth, there is an apparent decrease in focal gain with increasing Q, as depicted in Fig. 7. This decrease is attributed to a relatively broad transmit beam proximal and distal to the focal zone. The challenges associated with the short coherence lengths produced by a broad transmit beam outside of the focal region may be overcome by using a larger number of emission focal points, as demonstrated in Fig. 10, or by applying depth-dependent gain to the SLSC image.

Spatial compounding is a favored method for reducing speckle variance in ultrasound images, often performed at the expense of lateral resolution. Figs. 10(b) and 10(e) may be used to compare equivalent-sized receive apertures in SLSC and spatial-compounded images, respectively, and demonstrates a distinct difference between the two imaging modalities. The SNR of a homogeneous region in the thyroid improved by a factor of 2 in the spatial-compounded image compared with the B-mode image, whereas a factor of 3 improvement was achieved in the SLSC image. In addition, the apparent detail of the cyst is worse in the spatial-compounded image than in the comparable SLSC image, even though resolution is expected to differ by less than 0.2 mm, as estimated with Fig. 6(d).

The SLSC metric differs from other coherence metrics in its calculation and in its direct application to image formation. However, it can be utilized like other coherence metrics. The primary proposed use of the GCF and PCF coherence metrics developed by Li and Li [11] and Camacho *et al.* [14] was to weight B-mode data. Like these metrics, the SLSC value can be used to weight the B-mode image rather than form a direct image of SLSC values. In this case, speckle will be present in the weighted image and the anticipated benefits in CNR and SNR would be lost in favor of improved contrast.

One notable limitation of SLSC imaging is its inability to detect point-like targets in speckle-based background. The point targets in SLSC images of Fig. 2 are not present because the coherence of speckle is similar to that of the point target for short lags. Clinical tasks that depend on point target conspicuity, such as microcalcification detection, will be difficult with SLSC imaging.

A potential application of SLSC imaging is to reduce clutter, particularly in cardiovascular or abdominal imaging. Fig. 10 demonstrates that SLSC imaging is the preferred technique in the presence of clutter or other noise sources that corrupt diagnostic information. The SLSC images of Fig. 10 have 20 to 30 dB more contrast than corresponding B-mode images because of reduced clutter inside the anechoic cyst. Such large contrast improvements are not observed in simulated data when the simulated noise level is lower than the magnitude of noise present in the thyroid images. Although the simulation analysis does not include the influence of clutter on B-mode and SLSC images, the experimental thyroid data reveal that SLSC imaging yields greater clutter suppression than B-mode imaging.

As mentioned in Section I, the shape of a transmit beam influences the spatial coherence of backscattered echoes. For example, a change in the transmit aperture apodization alters the transmit beam shape and thus alters the expected spatial coherence function [as predicted by (5)] and the resulting SLSC image. It is likely that optimal apodization for SLSC imaging differs from the typical apodization used in B-mode imaging.

The challenges for real-time implementation of SLSC imaging are similar to the challenges associated with phase aberration correction and adaptive (or data-dependent) beamforming methods. For example, access to the channel signals is required in these approaches and is influenced by the ultrasound system's ability to provide such signals. In addition, the computational complexity of SLSC imaging is far greater than delay-and-sum beamforming. SLSC imaging uses many more cross correlations than phase aberration correction techniques, but is on par with the amount used in more advanced adaptive beamforming methods [33]. SLSC would likely be easily realized on software-based beamformers.

VI. Conclusion

We have developed an imaging technique based on the spatial coherence of ultrasound signals, with potential applications to clutter reduction. The spatial coherence between closely-spaced elements may be used to create images having the potential to compete with conventional B-mode images. SLSC images demonstrate inferior point target conspicuity compared with B-mode imaging, but show superior SNR and CNR as demonstrated in simulation, tissue-mimicking phantom, and *in vivo* human thyroid experiments. In expanded targets, a recorrelation effect is observed in theoretical and simulated results without noise. However, when noise is present, this recorrelation effect is mitigated, as demonstrated in experimental results and simulations with added noise.

SLSC images demonstrate a trade-off among contrast, CNR, and SNR with increasing short-lag values. SLSC imaging shows improved resolution with increasing lag and demonstrates better resolution than B-mode imaging for comparatively same-sized transmit apertures. The *in vivo* application of SLSC imaging to human thyroid tissue shows images that are substantially better than conventional speckle-reduction techniques, in addition to having better contrast, CNR, and SNR than B-mode images.

References

[1] J. W. Goodman, *Statistical Optics*. New York, NY: Wiley-Interscience, 2000.

[2] R. Mallart and M. Fink, "The van Cittert–Zernike theorem in pulse echo measurements," *J. Acoust. Soc. Am.*, vol. 90, no. 5, pp. 2718–2727, 1991.

[3] D. Liu and R. Waag, "About the application of the van Cittert-Zernike theorem in ultrasonic imaging," *IEEE Trans. Ultrason. Ferroelectr. Freq. Control*, vol. 42, no. 4, pp. 590–601, 1995.

[4] W. Walker and G. Trahey, "Speckle coherence and implications for adaptive imaging," *J. Acoust. Soc. Am.*, vol. 101, no. 4, pp. 1847–1858, 1997.

[5] J. Bamber, R. Mucci, and D. Orofino, "Spatial coherence and beamformer gain," *Acoust. Imaging*, vol. 24, pt. 1, pp. 43–48, 2000.

[6] J. Bamber, R. Mucci, D. Orofino, and K. Thiele, "B-mode speckle texture: The effect of spatial coherence," *Acoust. Imaging*, vol. 24, pt. 1, pp. 141–146, 2000.

[7] W. Walker and G. Trahey, "The application of k-space in pulse echo ultrasound," *IEEE Trans. Ultrason. Ferroelectr. Freq. Control*, vol. 45, no. 3, pp. 541–558, 1998.

[8] R. Mallart and M. Fink, "Adaptive focusing in scattering media through sound-speed inhomogeneities: The van Cittert Zernike approach and focusing criterion," *J. Acoust. Soc. Am.*, vol. 96, no. 6, pp. 3721–3732, 1994.

[9] B. Geiman, R. Gauss, and G. Trahey, "In vivo comparison of fundamental and harmonic lateral transmit beam shapes," in *2000 IEEE Ultrasonics Symp.*, vol. 2, pp. 1669–1675.

[10] K. W. Hollman, K. W. Rigby, and M. O'Donnell, "Coherence factor of speckle from a multi-row probe," in *Proc. 1999 IEEE Ultrasonics Symp.*, vol. 2, pp. 1257–1260.

[11] P. Li and M. Li, "Adaptive imaging using the generalized coherence factor," *IEEE Trans. Ultrason. Ferroelectr. Freq. Control*, vol. 50, no. 2, pp. 128–141, 2003.

[12] K. F. Ustuner, P.-C. Li, M.-L. Li, T. L. Thomas, and A. Gee, "Coherence factor adaptive ultrasound imaging methods and systems," U. S. Patent 7744532, Jun. 29, 2005.

[13] D. Liu and R. Waag, "Correction of ultrasonic wavefront distortion using backpropagation and a reference waveform method for time-shift compensation," *J. Acoust. Soc. Am.*, vol. 96, no. 2, pt. 1, pp. 649–660, 1994.

[14] J. Camacho, M. Parrilla, and C. Fritsch, "Phase coherence imaging," *IEEE Trans. Ultrason. Ferroelectr. Freq. Control*, vol. 56, no. 5, pp. 958–974, 2009.

[15] M. A. Lediju, M. J. Pihl, J. J. Dahl, and G. E. Trahey, "Quantitative assessment of the magnitude, impact, and spatial extent of ultrasonic clutter," *Ultrason. Imaging*, vol. 30, no. 3, pp. 151–168, 2008.

[16] M. A. Lediju, M. J. Pihl, S. J. Hsu, J. J. Dahl, C. M. Gallippi, and G. E. Trahey, "A motionbased approach to abdominal clutter reduction," *IEEE Trans. Ultrason. Ferroelectr. Freq. Control*, vol. 56, no. 11, pp. 2437–2449, 2009.

[17] M. O'Donnell and S. Flax, "Phase aberration measurements in medical ultrasound: Human studies," *Ultrason. Imaging*, vol. 10, no. 1, pp. 1–11, 1988.

[18] S. Bjaerum, H. Torp, and K. Kristoffersen, "Clutter filter design for ultrasound color flow imaging," *IEEE Trans. Ultrason. Ferroelectr. Freq. Control*, vol. 49, no. 2, pp. 204–216, Feb. 2002.

[19] G. Zwirn and S. Akselrod, "Stationary clutter rejection in echocardiography," *Ultrasound Med. Biol.*, vol. 32, no. 1, pp. 43–52, Jan. 2006.

[20] S. Miyashita, "Efficacy of dynamic flow ultrasonography in fetal vascular imaging," *Med. Rev*, vol. 27, no. 3, pp. 20–25, 2003.

[21] R. Entrekin, P. Jackson, J. Jago, and B. Porter, "Real time spatial compound imaging in breast ultrasound: Technology and early clinical experience," *Medicamundi*, vol. 43, no. 3, pp. 35–43, Sep. 1999.

[22] S. Huber, M. Wagner, M. Medl, and H. Czembirek, "Real-time spatial compound imaging in breast ultrasound," *Ultrasound Med. Biol.*, vol. 28, no. 2, pp. 155–163, 2002.

[23] R. J. Fedewa, K. D. Wallace, M. R. Holland, J. R. Jago, G. C. Ng, M. R. Rielly, B. S. Robinson, and J. G. Miller, "Spatial coherence of the nonlinearly generated second harmonic portion of backscatter for a clinical imaging system," *IEEE Trans. Ultrason. Ferroelectr. Freq. Control*, vol. 50, no. 8, pp. 1010–1022, 2003.

[24] J. A. Jensen, "Field: A program for simulating ultrasound systems," in *10th Nordic-Baltic Conf. Biomedical Imaging*, vol. 4, suppl. 1, pt. 1, pp. 351–353, 1996. [Online]. Available: http://server.electro.dtu.dk/personal/jaj/field/

[25] J. J. Dahl, M. S. Soo, and G. E. Trahey, "Spatial and temporal aberrator stability for real-time adaptive imaging," *IEEE Trans. Ultrason. Ferroelectr. Freq. Control*, vol. 52, no. 9, pp. 1504–1517, 2005.

[26] J. J. Dahl, D. A. Guenther, and G. E. Trahey, "Adaptive imaging and spatial compounding in the presence of aberration," *IEEE Trans. Ultrason. Ferroelectr. Freq. Control*, vol. 52, no. 7, pp. 1131–1144, 2005.

[27] S. S. Brunke, M. F. Insana, J. J. Dahl, C. Hansen, M. Ashfaq, and H. Ermert, "An ultrasound research interface for a clinical system," *IEEE Trans. Ultrason. Ferroelectr. Freq. Control*, vol. 54, no. 1, pp. 198–210, 2007.

[28] S. Smith and H. Lopez, "A contrast-detail analysis of diagnostic ultrasound imaging," *Med. Phys.*, vol. 9, no. 1, p. 4–12, 1982.

[29] K. R. Nightingale, M. S. Soo, R. W. Nightingale, and G. E. Trahey, "Acoustic radiation force impulse imaging: In vivo demonstration of clinical feasibility," *Ultrasound Med. Biol.*, vol. 28, no. 2, pp. 227–235, 2002.

[30] J. J. Dahl, D. M. Dumont, E. M. Miller, J. D. Allen, and G. E. Trahey, "Acoustic radiation force impulse imaging for noninvasive characterization of carotid artery atherosclerotic plaques: A feasibility study," *Ultrasound Med. Biol.*, vol. 35, no. 5, pp. 707–716, 2009.

[31] R. Righetti, J. Ophir, and P. Ktonas, "Axial resolution in elastography," *Ultrasound Med. Biol.*, vol. 28, no. 1, pp. 101–113, 2002.

[32] S. Srinivasan, R. Righetti, and J. Ophir, "Trade-offs between the axial resolution and the signalto-noise ratio in elastography," *Ultrasound Med. Biol.*, vol. 29, no. 6, pp. 847–866, 2003.

[33] Z. Wang, J. Li, and R. Wu, "Time-delay-and time-reversal-based robust capon beamformers for ultrasound imaging," *IEEE Trans. Med. Imaging*, vol. 24, no. 10, pp. 1308–1322, 2005.

Muyinatu A. Lediju was born on August 3, 1984 in Brooklyn, NY. She studied at the Massachusetts Institute of Technology, where she earned her B.S. degree in mechanical engineering with a minor in biomedical engineering in 2006. She is currently a Ph.D. candidate in biomedical engineering at Duke University. Her research interests include coherence-based imaging, ultrasonic clutter, multidemensional motion tracking, echocardiography, and medical instrumentation design.

Gregg E. Trahey (S'83–M'85) received the B.G.S. and M.S. degrees from the University of Michigan, Ann Arbor, MI, in 1975 and 1979, respectively. He received the Ph.D. degree in biomedical engineering in 1985 from Duke University, Durham, NC. He served in the Peace Corps from 1975 to 1978, and was a project engineer at the Emergency Care Research Institute in Plymouth Meeting, PA, from 1980 to 1982. He is a professor with the Department of Biomedical Engineering, Duke University. He is conducting research in adaptive phase correction, radiation force imaging methods, and 2-D flow imaging in medical ultrasound.

Brett C. Byram is a graduate student in the Biomedical Engineering Department at Duke University, Durham, NC, working towards the Ph.D. degree. He received the B.S. degree in Biomedical Engineering and Math in 2004 from Vanderbilt University, Nashville, TN. He is a graduate of the National Outdoor Leadership School and a member of the Society of Duke Fellows. His ultrasound research interests include beamforming and motion estimation.

Jeremy J. Dahl was born in Ontonagon, MI, in 1976. He received the B.S. degree in electrical engineering from the University of Cincinnati, Cincinnati, OH, in 1999. He received the Ph.D. degree in biomedical engineering from Duke University in 2004. He is currently an Assistant Research Professor with the Department of Biomedical Engineering at Duke University. His research interests include adaptive beamforming, noise in ultrasonic imaging, and radiation force imaging methods.